PROCEEDINGS, Thirty-Sixth Workshop on Geothermal Reservoir Engineering
Stanford University, Stanford, California, January 31 - February 2, 2011
SGP-TR-191

# 3D ANALYSIS OF HUFF AND PUFF AND INJECTION TESTS IN GEOTHERMAL RESERVOIRS

M.R. Safari and A. Ghassemi

Department of Petroleum Engineering at Texas A&M University
College Station, Texas, U.S.A

e-mail: ahmad.ghassemi@pe.tamu.edu

## ABSTRACT

Heat extraction from deep, hot rocks for energy production is based on water circulation through a man made fracture or natural fractures. As multiple and non-planar fractures in a stress field affect the geothermal reservoir behavior, so the capability to simulate multiple fractures and joints is needed to help reservoir design and operation. A 3D model is developed in this work to simulate and analyze a faulted and fractured deep rock mass subjected to fluid injection. The three-dimensional displacement discontinuity method is used for the fractures and joints, and Galerkin Finite Element method is used to represent flow equation within the fractures. The model is applied to analyze the pressure history data during cyclic injection/extraction (huff and puff) of a geothermal reservoir. Good agreement is observed between numerical results and field measurements. Additionally, an example is presented to highlight the versatility of the method, and to study the role of injection and the stress field on fracture slip and induced micro seismic events.

## INTRODUCTION

When designing geothermal reservoirs, the impedance factor, water loss rate, and availability of an adequately large heat exchange surface between rock and circulating fluid are considered to control the economic viability of heat extraction operations (Baria et al. 1999; Rutqvist et al. 2003). As the fractures are the major pathway for fluid flow and heat exchange, analysis of their spatial-temporal behavior has been the focus of many investigations, which have shown that coupled poro-mechanical, thermal, and geochemical process have a large influence on fracture permeability evolution. Generally, predicting the impact of the interactions of these processes, and interactions between natural fractures and man-made fracture requires numerical modeling. During past decades, various numerical models have been developed and used in reservoir simulators.

Wessling et al.(Wessling et al. 2009) simulated water injection into a fracture using 2.D-ROCMAS finite element software which has a coupled flow-geomechanic capability. Mathias et al.(Mathias et al. 2010) modeled the problem without any coupling between hydrological and mechanical processes and assumed a constant total stress and fracture aperture during injection/extraction cycles. Swenson et al. (Swenson 1992) developed a finite-element model to solved the problem using a 2D finite element method by assuming 1D fluid flow and constant joint stiffness. The displacement discontinuity method has proven to be particularly effective for the class of problems involving a finite number of discrete fractures within the circulation system.

Ghassemi et al. (Ghassemi et al. 2003; Ghassemi et al. 2005; Ghassemi et al. 2007) presented 3D boundary integral equation methods to investigate the coupled thermo- stresses in the injection/extraction problem while accounting for the natural fracture response using a linear joint model. Combined poro- and thermoelastic process were then considered (Zhou et al. 2009). Here, we extend this work and develop a general numerical algorithm to model injection/extraction problems in pre-existing or induced sets of fractures for variable injection/extraction rates. The model uses a coupled finite element/boundary element method to solve for fluid flow and fracture aperture in the fractures/matrix system. The displacement discontinuity method is used to consider the mechanical response of the fractures and multiple fracture interaction while considering the non-linear joint response.

## GOVERNING EQUATIONS

Behavior of fluid-saturated rocks is a transient phenomenon that can be described by the linear theory of poroelasticity (Biot 1941; Rice 1976). For isothermal condition, the poroelastic constitutive equation can be presented as:

$$\varepsilon_{ij} = \frac{1}{2G}\left[\sigma_{ij} - \frac{\nu}{1+\nu}\sigma_{kk}\delta_{ij}\right] + \frac{\alpha(1-2\nu_u)}{2G(1+\nu)}\delta_{ij}p \qquad (1)$$

$$\zeta = \frac{\alpha(1-2\nu)}{2G(1+\nu)}\sigma_{kk} + \frac{\alpha^2(1-2\nu)^2(1+\nu_u)}{2G(1+\nu)(\nu_u-\nu)}p \qquad (2)$$

Where $\varepsilon_{ij}$ and $\sigma_{ij}$ are correspondingly strain and stress of rock structure, $p$ and $\zeta$ are correspondingly pore pressure and diffused pore volume, $\delta_{ij}$ is Kronecker delta. G is the shear modulus, $\alpha$ is Biot effective stress coefficient. Drained $\nu$, and undrained Poisson's ratio $\nu_u$, and Skempton parameter B are other material constants (a set of 5 independent constant is sufficient).

Equations (1) and (2) state, respectively, the relation between the volumetric response of the rock and the pore pressure variation, and the change in pore pressure in response to an applied mean stress.

Pore-fluid diffusion equation can be considered by Darcy's law;

$$q_i' = -\frac{k}{\mu}p_{,i} \qquad (3)$$

This equation relates fluid mass flow in each direction and unit area to the gradient of pressure in the same path, where $q_i'$ is fluid flux in i-direction, is base permeability, and $\mu$ is viscosity of pore fluid.

By utilizing equation (1), (2), and (3) with equilibrium and compatibility condition, three-dimensional field equations can be obtained. The Navier's equations with a pore pressure coupling and the diffusion equation are:

$$G\nabla^2 u_i + \frac{G}{1-2\nu}u_{k,ki} - \alpha\nabla p = 0$$

$$\frac{\partial p}{\partial t} - \frac{2kGB^2(1-2\nu)(1+\nu_u)^2}{9\mu(\nu_u-\nu)(1-2\nu_u)}\nabla^2 p = -\frac{2GB(1+\nu_u)}{3(1-2\nu_u)}\frac{\partial \varepsilon}{\partial t} \qquad (4)$$

where $u_i$ is the solid displacement in the i-direction, $\varepsilon$ is the volumetric strain, and the other terms are the same as previous formulation. These equations should be solved with appropriate boundary conditions. At infinity, the in-situ stress and pore pressure conditions are prescribed for each time step. For an open fracture or closed joint, the boundary condition can be presented as:

For Closed Joint:

$$\sigma'(x,y,z,t) = \sigma(x,y,z,t) - \alpha\, p(x,y,z,t)$$

$$\alpha_{\text{joint}} = 1.0$$

For Open Fracture: (5)

$$\sigma(x,y,z,t) = p(x,y,z,t)$$

where $p(x,y,z,t)\big|_{@\text{ joint/crack location}}$ = Pressure on joint surfaces at each time $= \{p(x,y,0,t) \quad x,y \in A\}$

For fluid flow modeling between fracture surfaces, it is supposed that laminar flow occurs as described by the following lubrication equation(Zhou et al. 2009):

$$\nabla p(x,y,z,t) = -\frac{12}{w^3(x,y,z)}q(x,y,z,t) \quad x,y,z \in A \qquad (6)$$

where $w(x,y,z)$ and $q(x,y,z,t)$ are the fracture aperture and fluid discharge into the matrix from fractures wall, respectively. Assuming that the water injected into the fractures is incompressible and the joint aperture is variable with time, the fluid mass continuity equation can be presented as:

$$\nabla q(x,y,z,t) =$$

$$-2\upsilon_l(x,y,z,t) + Q_{inj}(t)\delta(x-x_{inj}, y-y_{inj}, z-z_{inj}) \qquad (7)$$

$$-Q_{ext}(t)\delta(x-x_{ext}, y-y_{ext}, z-z_{ext}) - \frac{\partial w(x,y,z)}{\partial t}$$

where $\upsilon_l(x,y,z,t)$ is amount of leak off from one surface of fractures into rock matrix, $Q_{inj}(t)$ and $Q_{ext}(t)$ are cold water injection and hot water extraction rate, respectively, and $\delta(x,y,z)$ is Dirac delta function. Equation (6) and (7) can be written in the form:

$$\nabla\left[w^3(x,y,z)\nabla p(x,y,z,t)\right] =$$

$$12\mu\begin{bmatrix} 2\upsilon_l(x,y,z,t) - Q_{inj}(t)\times \\ \delta(x-x_{inj}, y-y_{inj}, z-z_{inj}) + Q_{ext}(t)\times \\ \delta(x-x_{ext}, y-y_{ext}, z-z_{ext}) + \dfrac{\partial w(x,y,z)}{\partial t} \end{bmatrix} \qquad (8)$$

In this equation the pressure on fracture surfaces and leak off into the rock matrix are not known. They can be solved for a given history of injecting and extracting rates at the wells. Another boundary condition is:

$$\frac{\partial p}{\partial n} = 0 \quad on \quad \partial A \qquad (9)$$

where $n$ is the outer normal to the edge of fracture surfaces. This boundary condition implies perpendicular direction of pressure on fractures surfaces.

## INTEGRAL SOLUTION METHOD

To analyze geothermal reservoirs with multiple fractures during arbitrary injection/extraction period, equations (4) and (8) should be solved simultaneously with respect to all boundary conditions (Equations (5) and (9)). It is obvious that these two equations are coupled through fracture surfaces pressure and fracture aperture. The DD methods and Galerkin finite element method are used to discretized equation (4) and (8), respectively.

Fractures in poroelastic rock can be seen as a surface across which, the solid displacements and the normal fluid flux are discontinuous, and the tractions depend on the normal and shear displacements and amount of fluid source (leak-off) from fractures surfaces. The DDs and fluid sources are distributed along the joint wall such that the summation of their effects satisfies the boundary conditions at joint surfaces. The stresses and pressures at any point in the rock matrix can be evaluated by using discontinuity of displacement and fluid flux:

$$\sigma_{ij}(X,t_n) = \int_0^{t_n}\int_A \begin{Bmatrix} \sigma_{ijkn}^{id}(X-X',t-t')D_{kn}(X',t') + \\ \sigma_{ij}^{is}(X-X',t-t')D_f(X',t') \end{Bmatrix} dA(X')\,dt' + \sigma_{ij}(X,0) \quad (10)$$

$$p(X,t_n) = \int_0^{t_n}\int_A \begin{Bmatrix} p_{ij}^{id}(X-X',t-t')D_{ij}(X',t') + \\ p^{is}(X-X',t-t')D_f(X',t') \end{Bmatrix} dA(X')\,dt' + p(X,0) \quad (11)$$

where $D_{ij}$ and $D_f$ are respectively the displacement discontinuity components and the fluid source intensity or fluid discharge to the rock matrix. $\sigma_{ijkn}^{id}$, $\sigma_{ij}^{is}$, $p_{ij}^{id}$ and $p^{is}$ are the instantaneous fundamental solution of the stresses and pore pressure due to a unit impulse of the displacement discontinuity (superscript "id") and a unit impulse of fluid discharge from surface of fracture ("is"); and $\sigma_{ij}(X,0)$, $p(X,0)$ are the initial value of stresses (in-situ stresses) and background pore pressure. Equations (10) and (11) are applied on all fracture surfaces to get the DDs and fluid discharge. As the DDs and fluid source intensities at fracture surfaces are defined, equations (10) and (11) can then be used to calculate the stresses and pore pressure at any location in the rock matrix. The convolution algorithm is used for the temporal domain integrals involving continuous DDs and fluid source fundamental solutions.

The integrals of instantaneous fundamental solutions in time domain can be expressed in terms of corresponding continuous fundamental solutions to develop the convolution time integrals by going back to zero at every time step. In this way, domain integration is circumvented. After applying continuous approach to the equations, three traction component on every fracture surface is extracted from equation (10). Equation (11) and discretized form of equation (8) are the other two equations, in addition to these three traction equations. Totally there are eight unknowns in these five equation set, and three more relation is needed for complete solution. These three equations are fractures behavior model for normal and shear displacements.

If two surfaces of fracture separate from each other, or if just a part of surface separates, the shear stress is set to zero and the normal stress equals the pressure on fracture surface. When the two surfaces are compressed together, the fracture behaves as a closed joint with a nonlinear behavior (Goodman 1974). When closed, the fracture surfaces can tolerate shear forces. The shear displacement-shear force behavior is considered to be elastic-perfectly plastic, and the threshold for constant shear force on fracture is defined by using Mohr-Coulomb criteria.

The normal opening behavior of joint can be written as(Goodman 1974);

$$\Delta(\sigma_n') = K_n\,\Delta(DD_n) \quad (12)$$

where $\sigma_n'$ is effective stress and can be present as;

$$\sigma_n' = \sigma_n - p \quad (13)$$

From Goodman(Goodman 1974) it can be seen that the discontinuity behavior is presented as:

$$\frac{\sigma_n' - \sigma_n'^0}{\sigma_n'^0} = A\left(\frac{\Delta a}{a_0 - \Delta a}\right)^t \quad (14)$$

where A and t are fitted parameter. Similarly to (Wessling et al. 2009; Mathias et al. 2010) it is assumed that A and t equal 1.0, therefore, the behavior simplified to:

$$\sigma_n' a = \sigma_n'^0 a_0 \quad (15)$$

where $a_0$ is initial joint aperture at initial effective stress at joint surface ($\sigma_n'^0$).

Now with the above three fracture force-displacement model equations, the problem can be solved to find the discontinuities and other unknowns on the joint surfaces.

## NUMERICAL SOLUTION

As it was mentioned before, Galerkin finite element method is used to model fluid flow in joint(Zhou et

al. 2009). Joint plane is discretized into M elements, and it is considered that:

$$p^{(m)} = \mathrm{N}^{(m)}\tilde{\mathrm{p}}, \qquad q_f{}^{(m)} = \mathrm{N}^{(m)}\tilde{\mathrm{q}}_f \tag{16}$$

where $\mathrm{N}^{(m)}$ are the interpolative functions, the superscript "m" indicate the number of element, and $\tilde{\mathrm{p}}$ and $\tilde{\mathrm{q}}_f$ are the vectors of nodal fluid pressure and fluid source intensity, in that order. By using Galerkin FEM, equation (8) can be written as(Zhou et al. 2009):

$$\mathrm{A}_1\tilde{\mathrm{p}}(\mathrm{t}) + \mathrm{A}_2\,\tilde{\mathrm{q}}_\mathrm{f}(\mathrm{t}) = \mathrm{B}_1(\mathrm{t}) \tag{17}$$

Where:

$$\mathrm{A}_1 = \sum_{m=1}^{M}\int_{A_e} \nabla^T \mathrm{N}^{(m)}\,\frac{w^3(x,y)}{12\mu}\nabla \mathrm{N}^{(m)} dA$$

$$\mathrm{A}_2 = \sum_{m=1}^{M}\int_{A_e} \mathrm{N}^{(m)\mathrm{T}}\mathrm{N}^{(m)} dA$$

$$\mathrm{B}_1 = \mathrm{N}^{(inj)\mathrm{T}}\Big|_{(x_{inj},y_{inj})} Q_{inj}(t) - \mathrm{N}^{(ext)\mathrm{T}}\Big|_{(x_{ext},y_{ext})} Q_{ext}(t) - \sum_{m=1}^{M}\int_{A_e} \mathrm{N}^{(m)\mathrm{T}}\frac{\partial w}{\partial t} dA$$

in which $\mathrm{N}^{(inj)}\Big|_{(x_{inj},y_{inj})}$ indicates the shape functions at the fluid injection well, which is located at $(x_{inj}, y_{inj})$ within element "inj", and $\mathrm{N}^{(ext)}\Big|_{(x_{ext},y_{ext})}$ denotes the shape function at the fluid extraction point, which is located at $(x_{ext}, y_{ext})$ within element "ext".

The same mesh for finite element and boundary element for all of fractures is used for space discretization. The joint is discretized into a number of four-nodded quadrilateral elements in the spatial domain, which makes the integrals over the whole fractures be replaced by a sum of integrals over these elements. The DDs are assumed to be constant over each element which facilitates the treatment of the hyper singular integrations involved; while the fluid source intensities are assumed to vary linearly over each element(equation (16)). In the time domain, the DDs and source intensities are assumed to be constant over each time step.

As all integrals are expressed in the intrinsic coordinates of the influenced plane element through coordinate transformation, the actual computation requires only a straightforward application of standard quadrature rules. We use Gaussian quadrature with 4×4 points for regular integral and 8×8 points for singular integral which ensures the accuracy for regular and hyper singular integrals. Finally, three traction equations from equation (10) and equation (11) is decritized and they can be represented as:

$$\begin{aligned}
\bar{\sigma}_1(\mathrm{t}) &= \mathrm{A}_{11}\bar{\mathrm{D}}_{33}(\mathrm{t}) + \mathrm{A}_{12}\bar{\mathrm{D}}_{13}(\mathrm{t}) + \mathrm{A}_{13}\bar{\mathrm{D}}_{23}(\mathrm{t}) + \mathrm{A}_{14}\mathrm{D}_\mathrm{f}(\mathrm{t}) + \mathrm{B}_1(\mathrm{t})\\
\bar{\sigma}_2(\mathrm{t}) &= \mathrm{A}_{21}\bar{\mathrm{D}}_{33}(\mathrm{t}) + \mathrm{A}_{22}\bar{\mathrm{D}}_{13}(\mathrm{t}) + \mathrm{A}_{23}\bar{\mathrm{D}}_{23}(\mathrm{t}) + \mathrm{A}_{24}\mathrm{D}_\mathrm{f}(\mathrm{t}) + \mathrm{B}_2(\mathrm{t})\\
\bar{\sigma}_3(\mathrm{t}) &= \mathrm{A}_{31}\bar{\mathrm{D}}_{33}(\mathrm{t}) + \mathrm{A}_{32}\bar{\mathrm{D}}_{13}(\mathrm{t}) + \mathrm{A}_{33}\bar{\mathrm{D}}_{23}(\mathrm{t}) + \mathrm{A}_{34}\mathrm{D}_\mathrm{f}(\mathrm{t}) + \mathrm{B}_3(\mathrm{t})\\
p(\mathrm{t}) &= \mathrm{A}_{41}\bar{\mathrm{D}}_{33}(\mathrm{t}) + \mathrm{A}_{42}\bar{\mathrm{D}}_{13}(\mathrm{t}) + \mathrm{A}_{43}\bar{\mathrm{D}}_{23}(\mathrm{t}) + \mathrm{A}_{44}\mathrm{D}_\mathrm{f}(\mathrm{t}) + \mathrm{B}_4(\mathrm{t})
\end{aligned} \tag{18}$$

where $\mathrm{A}_{ij}$ s are the effect of all elements on local traction of each element on *i*-direction, or the effect of each element on fractures surfaces pressure. Also $B_i$ s are the effect of discontinuity history.

Those four relations in equation (18) and equation (17) construct a set of coupled equation which are needed to solve with respect to fracture Force-Displacement behavior. This solution will represent all component of displacement discontinuity and fluid source (leak off) amount on all fractures surface.

## EXAMPLES

To verify the model and to show its capability, two examples are presented. The first example is just presented to verify model, and the second one to show how the method is used to simulate multiple fractures in porous media which happen in natural reservoir.

### Problme 1

In this example, an actual Huff and Puff test is simulated. The field experiment was carried out in borehole Horstberg Z1, Lower Saxony in Germany geothermal field. The data for this field are from Wessling et al. (Wessling et al. 2009) and Mathias et.al.(Mathias et al. 2009) who used semi-analytical and FEM models to simulate the huff–puff test into a penny-shaped joint. The joints hydro-mechanical behavior is reflected in the downhole pressure history recorded during a huff–puff process. The huff–puff test involved a cyclic extraction/recovery test whereby 2500 $m^3$ of cold water was injected into a joint over 36h followed by 30h rest and five successive 15h extractions of between 443 and 523 $m^3$ of fluid, each separated by a 9h resting period (Wessling et al. 2009). Temperature of reservoir near the fracture changed about 16$^o$ C during the test. The joint model (Fig. 1) parameter and other properties are listed in Table 1.

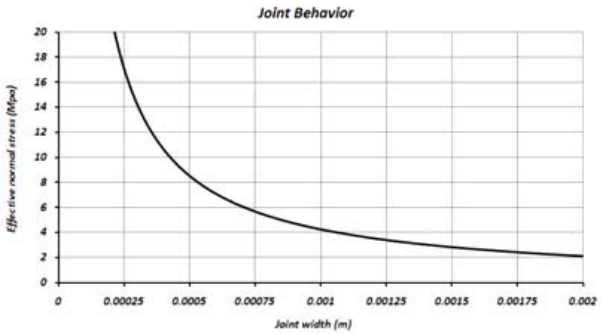


*Figure 1: Normal joint behavior.*

*Table 1: Joint and matrix characterization.*

| | |
|---|---|
| joint Radius (m) | 260 |
| Initial joint aperture (m) | 5.0E-4.0 |
| Initial pore pressure(MPa) | 60.0 |
| In-situ normal stress(MPa) | 68.5 |
| Biot's constant | 1.0 |
| Biot's modulus (GPa) | 44.0 |
| Rock permeability($m^2$) | $3.0\times10^{-17}$ |
| Young's modulus (GPa) | 6.0 |
| Drained Poisson's ratio | 0.25 |

Fig. 2 shows the joint mesh used in the simulation to analyze the variation of the pore pressure and stresses in the joint when water is injected/extracted into the circular joint; it contains 392 four-nodded quadrilateral elements and 372 nodes.

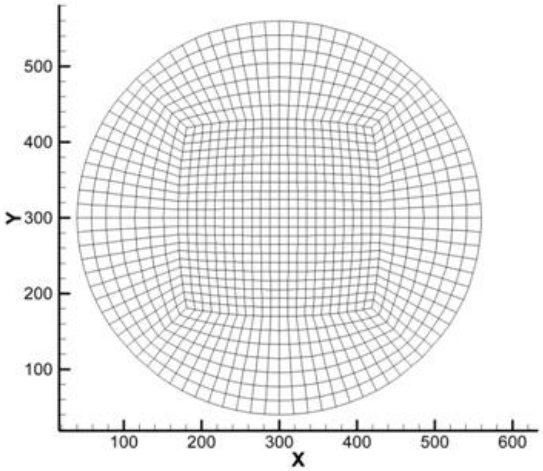


*Figure 2: Mesh used for circular joint.*

The pressure distribution in the joint at shut-in is shown in Fig. 3; as can be seen the distribution is uniform.

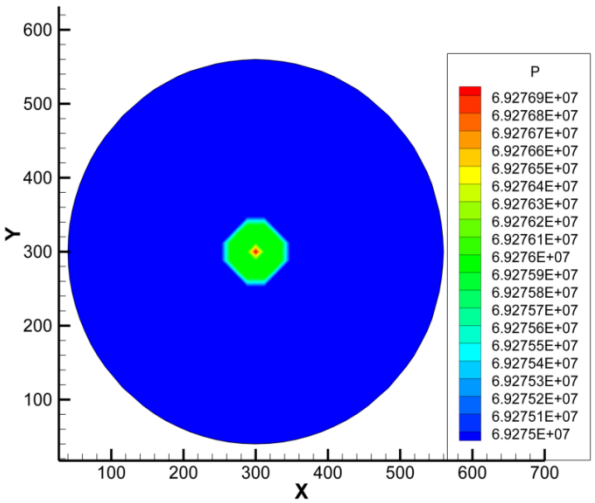


*Figure 3: Pressure(Pa) distribution at the beginning of shut-in phase (36 hours).*

The pressure history for the middle point of the joint is shown in Fig.4. The profile of the down hole pressure is in good agreement with the recorded data without any curve fitting and parameter optimization.

The differences between the field test and our numerical results can be attributed to the fact that a sandstone layer, which forms part of the joint wall near the center of joint with thickness of 4 m is not considered. It also assumed that the rock is homogeneous and isotropic. On the other hand, the difference between numerical results and the field test can be caused by uncertainty in rock parameters we used. It is important to note that the present method is highly sensitive to the joint model and its parameter as shown in the Fig. 4. The difference between the results for a linear normal stiffness case and the nonlinear Goodman joint is substantial. Overall, good agreement has been obtained between the simulated pressure profile and the measured field data indicating that the method can be successfully employed to investigate the injection/extraction in geothermal reservoirs.

Figs. 5-6 show the distribution of normal displacement discontinuity (DD) and effective stress plotted at end of the injection interval, at the first shut-in, and for production/shut-in phases in. As expected, the joint aperture decreases from its center toward the tip for every time step.

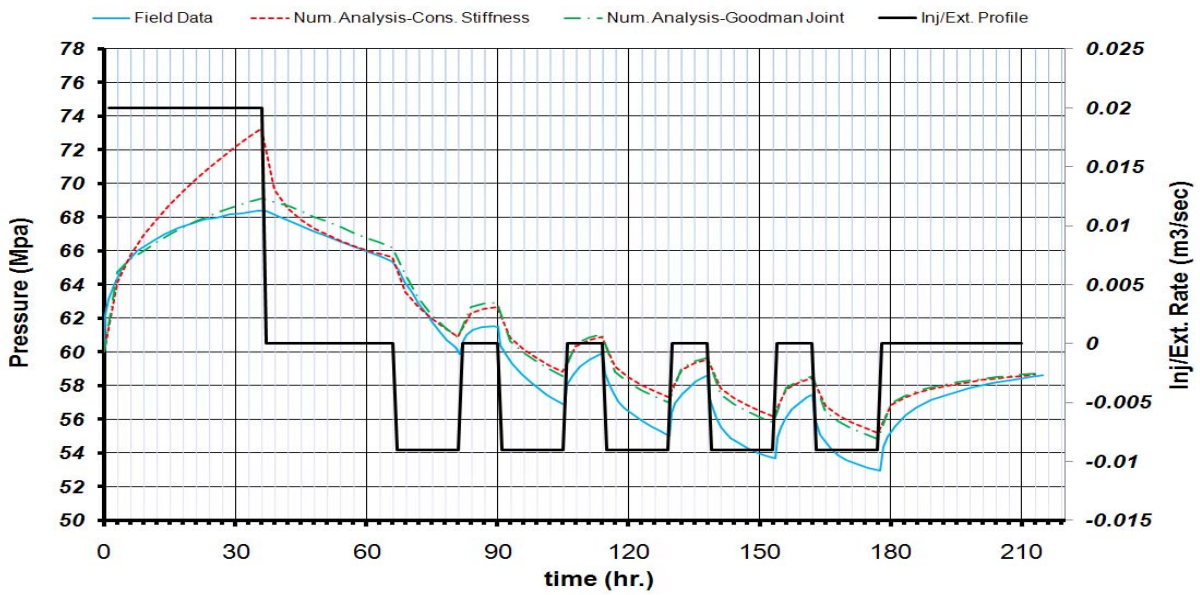


*Figure 4: Pressure profile at the well location during Huff and Puff test..*

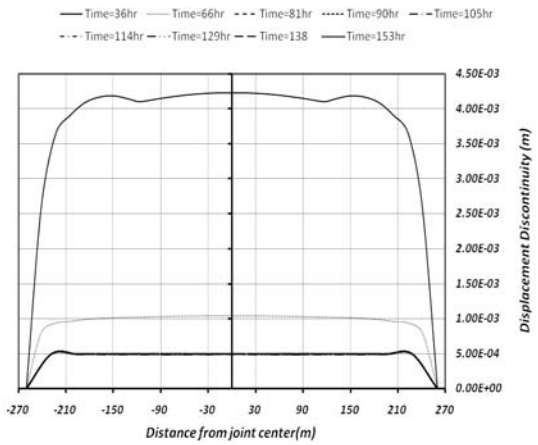


*Figure 5:Normal DD (aperture) along the fracture radius during huff and puff.*

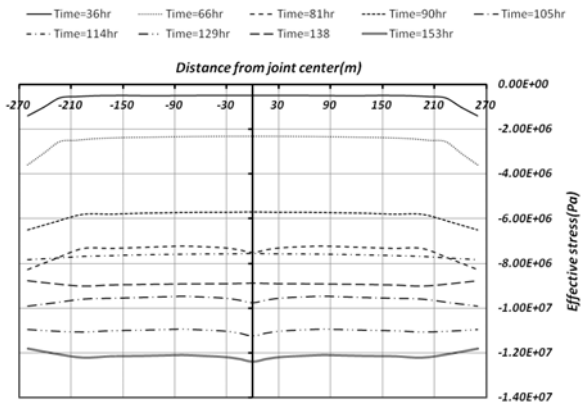


*Figure 6: Effective stress at different time steps.*

**Example 2**

In this example, we simulate a modified version of the injection experiment of Soultz-sous-Forets European Hot Fractured Rock Geothermal project, Rhine Garben, France, as reported by Bruel (Bruel 2002). This problem involves a number of fractures that were detected in the field and is a good example of the importance of the interactions between natural joints geometry and the in-situ stress field, and their impact on the evolution of permeability with injection. As in the previous case, we do not consider thermoelastic effects for the sake of simplifying the analysis. Also, the simulations are carried out for a relatively short time period, so that thermal effects have not fully developed.

Fig.7 shows the problem geometry and the location of the injection and extraction wells. General parameters and in-situ stress values are shown in Table 2. The stress state is one of normal faulting regime. Note that some of the fractures shown in (Bruel (2002) are not considered to save computational time. The variation of stress with space is not considered in this example.

It is assumed that the injection rate and extraction rates are equal to 1.0 lit/sec and 0.5 lit/sec, respectively. Also, it is assumed that before injection and extraction, all fractures are stable and because of in situ stress field, they are all mechanically closed, although they can be hydraulically open.

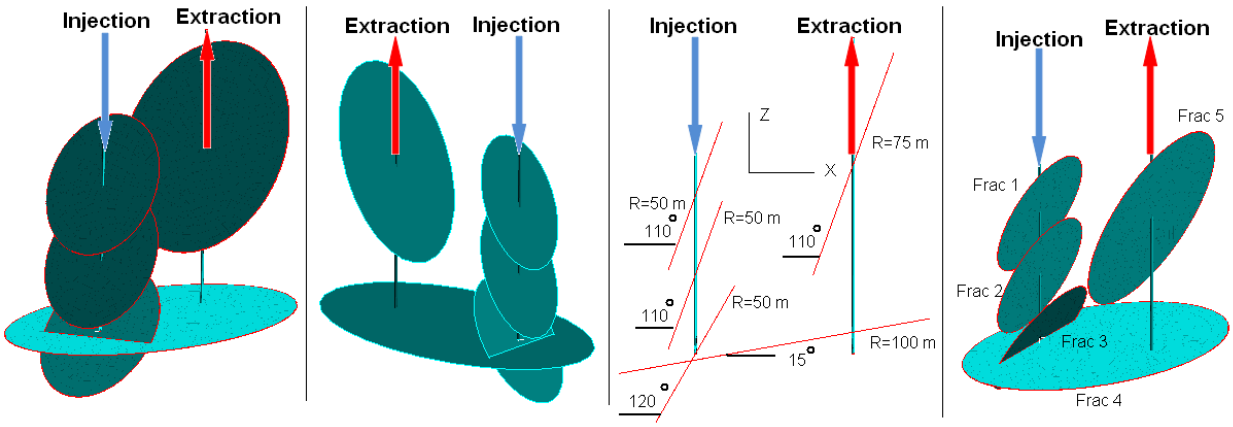


*Figure 7: Fracture network shown from different view direction (modified from (Bruel (2002).*

Figure 8 shows the status of the fractures prior to water injection. These fractures are discretized using 1814 four nodded elements with 1952 nodes. In this method, the well is simulated by applying the injection and extraction rates at the nodes where the well is located. Direction 1 refers in Fig.8 is along the dip on the fracture surface.

*Table 2: Multiple Fracture Modelling Parameters*

| | |
|---|---|
| X in situ stress (MPa) | 55.0 |
| Y in situ stress (MPa) | 50.0 |
| Z in situ stress (MPa) | 80.0 |
| Initial pore pressure(MPa) | 45.0 |
| Biot's constant | 1.0 |
| Biot's modulus (GPa) | 44.0 |
| Rock permeability($m^2$) | $3.0\times10^{-17}$ |
| Young's modulus (GPa) | 6.0 |
| Drained Poisson's ration | 0.25 |
| Initial joint aperture(m) | 5.0E-4.0 |
| Mohr-Coulomb, C (MPa) | 4.0 |
| Mohr-Coulomb, Friction angle | 27.0 |
| Dilation Angle | 3.0 |
| Initial Normal Stiffness (GPa/m) | 10.0 |
| Initial Shear Stiffness (GPa/m) | 10.0 |

It can be seen in Fig. 8 that fracture 4 has experienced minimum shear force along its dip, with a value of approximately 4 MPa. This is insufficient to cause slippage on this joint which is assumed to have a cohesive strength of 4MPa. Only joints number.1, 2, 3 and 5 experience sufficiently high shear stresses and can experience slip.

It should be mentioned that the negative shear stress along dip (1 direction) indicates that the shear acts in the up-dip direction. The shear stress component in the strike-direction of all fractures is zero.

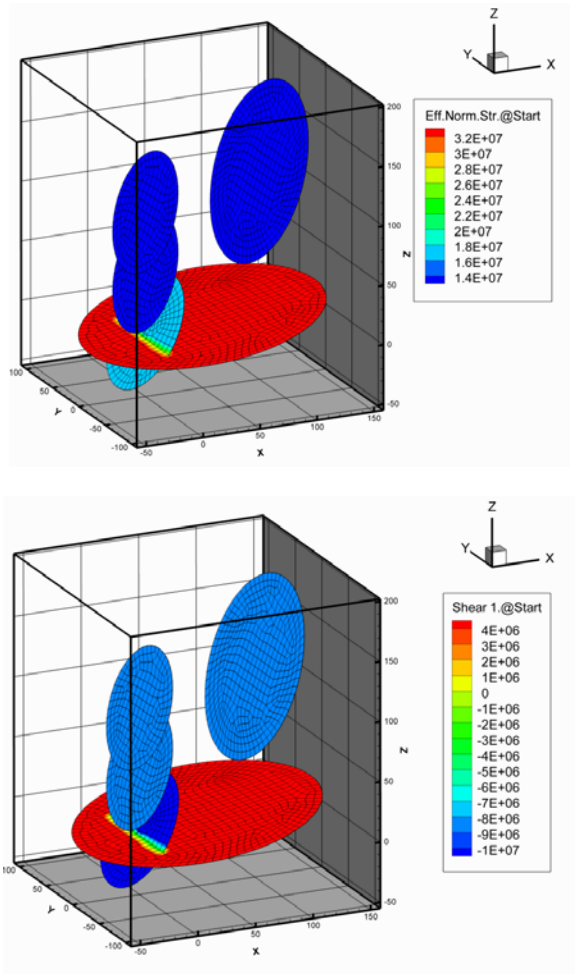


*Figure 8: Effective normal (top) and shear (bottom) stress on fractures, before starting injection or extraction.*

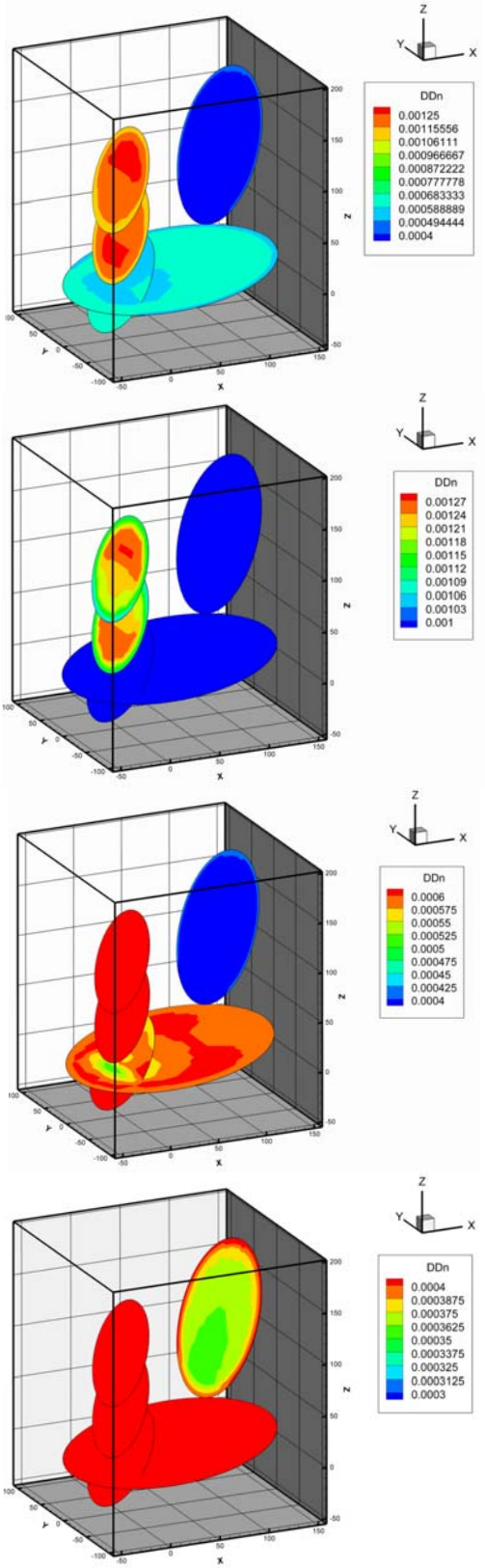


*Figure 9: Fracture aperture after 10 hours of injection and extraction. Note that each figure highlights the aperture on one fracture since the values have a broad range.*

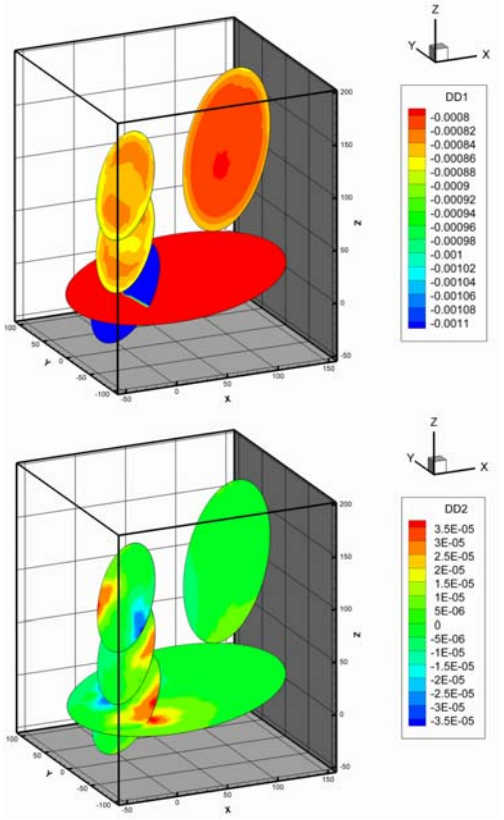


*Figure 10: Shear displacements on all fractures.*

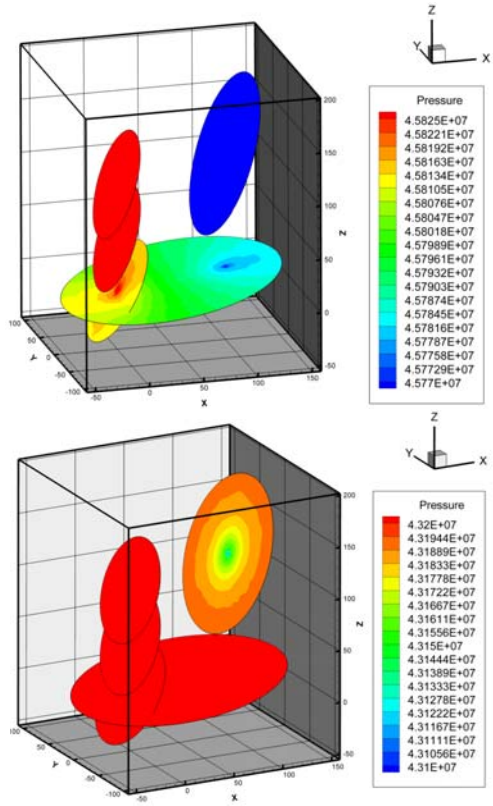


*Figure 11: Pressure distribution in the fractures after 10 hours of injection/extraction.*

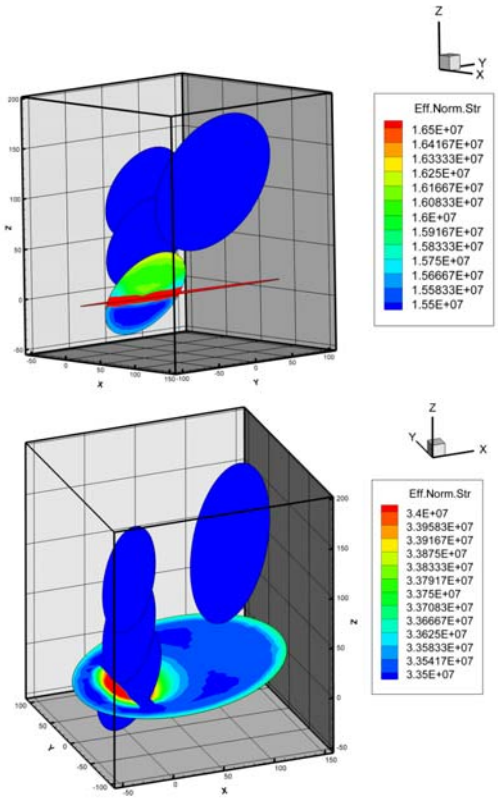


*Figure 12: Distribution of effective stress on fractures after 10 hours.*

The fracture aperture, shear displacement, and pressure distributions after 10 hours of operation are shown in Figures 9, 10 and 11. Because of the broad range of fractures aperture and pressure values in all fractures, multiple figures are used to illustrate the distribution of the parameters of interest for each fracture. As can be seen in Fig. 9, the aperture distribution on fracture 1 and 2 are in the same range of 1-1.3 mm. In addition, the aperture distribution for this set of fractures is nearly symmetric about the injection point. This is because they overlap, and the opening of one fracture induces some closure on the other one. The upper part of fracture 1 is less confined that the lower part, the reverse is true for the lower crack. The aperture of fractures 3 and 4 is in the range of 0.4 mm up to 0.6 mm. Because of contact between fracture 3 and 4, the aperture near is smaller near the intersection than in other parts. Fracture 4 has lower values of aperture because of fluid extraction from it.

The first part of Fig. 10 shows the shear displacement along the fracture dip. It can be seen that the maximum shear displacement is on fracture 3, because the maximum shear stress is exerted on it, due to stress field. On the second plot of Fig. 10, the shear displacement in the fracture strike direction is shown. Although, no in-situ shear stress is initially resolved in the strike direction of the fractures, the shear displacement on other fractures induces a shear movement in the strike-direction. This shear displacement along the strike is about 0.035 mm. These shear displacements are elastic and do not represent slippage that takes place when the joint stress exceeds its strength.

The pressure distributions on Fig.11 are consistent with the aperture distribution, Fig. 9. The pressure ranges from 43-68 MPa. Pressure in fractures 1 and 2 is about 67.6 MPa. The pressures do change in fracture 3, 4 and 5. Although, the amount of change is not much (0.1 MPa), but it has its effect on leak off from.

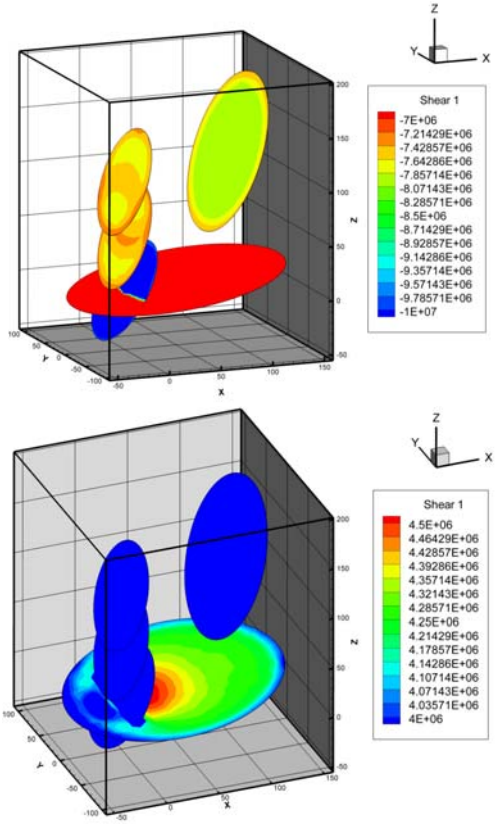


*Figure 13: Shear stress on all fractures in direction 1- Noted that direction 1 is not the same for all elements.*

Figure 12 shows the distribution of effective stress on fractures 3 and 4. It is interesting that effective stress on fracture 3 changes by about 1 MPa from top to the bottom. This shows that the part of fracture 3 which is below fracture 4 would slip before the upper part. The effective normal stress on fracture 4 varies from 33.5 MPa up to 34.5 MPa with the maximum stress occurring near where the two fractures intersect. This happens because of interaction with fracture 3 and its confining effect.

It is shown in Fig. 8 that the shear traction along dip of fracture 1 and 2 is about 8 MPa and while it is 10.8 MPa on fracture 3 (before the start of leak-off). Then, after 10 hours of operation, a certain amount of these shear stresses is released along the dip. It can be seen in Fig. 13, for example on fracture 1 and 2, the amount of shear stress decreases to 7.5 MPa after 10 hours.

## CONCLUSION

A three-dimensional poroelastic displacement discontinuity model has been developed for modeling coupled flow and fracture deformation for both natural and induced fractures in rock. The model combined the FE method to the DD method; it is poroelastic, and accounts for the geometric nonlinearity of the joint deformation, temporal variation of the injection/extraction rates, and pressure-dependent leak-off. The model has been applied to simulate field data from a Huff-Puff test. Good agreement has been obtained indicating that the method can be employed to investigate the variation of field parameters during injection/Extraction period in geothermal reservoirs. The example of multiple fractures in a reservoir rock illustrates the importance of fracture interactions on shear deformation and fracture slip. It also demonstrates the variation of permeability with injection and potential for induces seismicity resulting from slip on neighboring fractures. Such analysis also can shed light on direction of shear growth during reservoir development. Future analysis will consider the temperature of the extracted water as well as the influence of thermal stresses..

## REFERENCES


Baria, R., J. Baumgartner, et al. (1999). "HDR/HWR reservoirs: concepts, understanding and creation." *Geothermics* **28**: 533-552.

Biot, M. A. (1941). "General theory of three-dimensional consolidation." *Journal of Applied Physics* **12**(2): 155-164.

Bruel, D. (2002). "Impact des contraintes d'origine thermique lors d'un essai de circulation dans un réservoir géothermal développé en milieu fracturé : application au site de Soultz-sous-Forêts, Alsace, France, dans le cadre du projet européen sur la géothermie en milieu fracturé profond." *Oil & Gas Science and Technology - Rev. IFP* **57**(5): 459-470.

Ghassemi, A., S. Tarasovs, et al. (2003). "An integral equation solution for three-dimensional heat extraction from planar fracture in hot dry rock." *International Journal for Numerical and Analytical Methods in Geomechanics* **27**(12): 989-1004.

Ghassemi, A., S. Tarasovs, et al. (2005). "Integral equation solution of heat extraction-induced thermal stress in enhanced geothermal reservoirs." *International Journal for Numerical and Analytical Methods in Geomechanics* **29**(8): 829-844.

Ghassemi, A., S. Tarasovs, et al. (2007). "A 3-D study of the effects of thermomechanical loads on fracture slip in enhanced geothermal reservoirs." *International Journal of Rock Mechanics and Mining Sciences* **44**(8): 1132-1148.

Goodman, R. E. (1974). The mechanical properties of joints. *3rd International Congress of International Society of Rock Mechanics*, Denver, CO, USA.

Mathias, S. and M. van Reeuwijk (2009). "Hydraulic Fracture Propagation with 3-D Leak-off." *Transport in Porous Media* **80**(3): 499-518.

Mathias, S. A., C.-F. Tsang, et al. (2010). "Investigation of hydromechanical processes during cyclic extraction recovery testing of a deformable rock fracture." *International Journal of Rock Mechanics and Mining Sciences* **47**(3): 517-522.

Rice, J. R. (1976). "Some Basic Stress Diffusion Solutions for Fluid-Saturated Elastic Porous Media With Compressible Constituents." *Reviews of Geophysics and Space Physics* **14**: 227.

Rutqvist, J. and O. Stephansson (2003). "The role of hydromechanical coupling in fractured rock engineering." *Hydrogeology Journal* **11**(1): 7-40.

Swenson, D. (1992). An implicitly coupled model of fluid flow in jointed rock. *The 33th U.S. Symposium on Rock Mechanics (USRMS)*. Santa Fe, NM, A. A. Balkema, Rotterdam. Permission to Distribute - American Rock Mechanics Association.

Wessling, S., R. Junker, et al. (2009). "Pressure analysis of the hydromechanical fracture behaviour in stimulated tight sedimentary geothermal reservoirs." *Geothermics* **38**(2): 211-226.

Zhou, X. X., A. Ghassemi, et al. (2009). "A three-dimensional integral equation model for calculating poro- and thermoelastic stresses induced by cold water injection into a geothermal reservoir." *International Journal for Numerical and Analytical Methods in Geomechanics* **33**(14): 1613-1640.